Environmental and
Biogeochemical Processes

https://doi.org/10.48130/ebp-0026-0012

Original Research

Open Access

Alkyl carbon in a hydrophobic coating enhances the chemical stability of hydrochar

Jianping Fan[1], Fangfang Li[2*], Qingkong Chen[3], Peiwen Zeng[3], Yanlin Li[1], Wei Chen[1], Qiangbin Yang[1] and Hong Yang[4]

Received: 22 April 2026

Revised: 27 June 2026

Accepted: 13 July 2026

Published online: 17 August 2026

Abstract

Hydrochar has great potential in soil remediation, pollution control, and carbon sequestration. The hydrophobic coating formed on the surface of hydrochar may alter its function. For example, it is unclear how the formation and composition of this coating affect hydrochar stability. Here, hydrochar was produced from different plant leaves, and the difference in the composition of the hydrophobic coating and its effect on the thermal and chemical stability of hydrochar were investigated. Results showed that the hydrophobic coating on hydrochar derived from lotus leaves exhibited the greatest hydrophobic intensity, and its main composition was nonacosane-4,10-diol. The main composition of the hydrophobic coating on hydrochar derived from corn leaves, palm leaves, and pine needles was either palmitic acid or 16-hydroxypalmitic acid. The hydrophobic intensity of the coating was positively correlated with the alkyl carbon content of the bulk hydrochar. The removal of the coating did not alter the hydrochar's thermal stability, as this effect was counterbalanced by the concomitant increase in both activation energy and pre-exponential factor during thermal decomposition. Carbon loss of hydrochar oxidized by $K_2Cr_2O_7$ increased by 10.13%–16.01% after removing the hydrophobic coating. Therefore, the alkyl carbon contained in the hydrophobic coating could improve hydrochar stability in soil and raise its carbon sequestration potential.

Keywords: Hydrochar, Hydrophobic alkyl carbon, Hydrophobic coating, Stability, Plant cuticle

Highlights

- Hydrophobic alkyl carbon was the main composition of hydrophobic coating.
- Hydrophobic alkyl carbon of hydrophobic coating was derived from wax and cutin.
- Lotus leaf-derived hydrochar had the strongest hydrophobic coating.
- Hydrophobic coating reduced both *E* and *A* of hydrochar thermal decomposition.
- Hydrophobic alkyl carbon coating increased hydrochar chemical stability.

* Correspondence: Fangfang Li (fangkust@163.com)

Full list of author information is available at the end of the article.

https://doi.org/10.48130/ebp-0026-0012

Graphical abstract

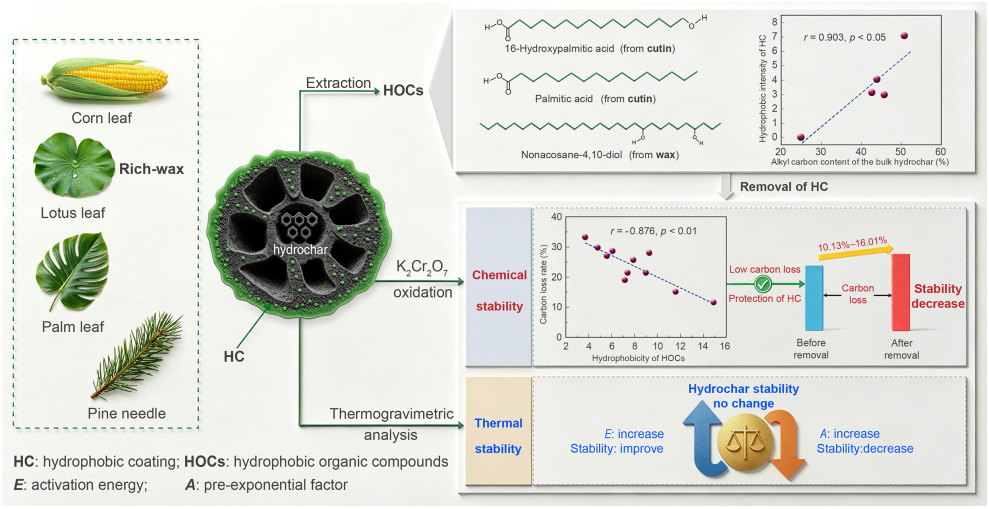

Introduction

Carbonization of biomass for carbon-rich materials is a technologically mature solution for achieving negative carbon emissions, which increases the soil carbon pool and crop yields[1]. The carbonization of biomass is commonly achieved through pyrolysis and hydrothermal carbonization. When the carbonization product (referred to as 'char') is added to soil, the readily degradable organic carbon in char stimulates the activity of soil microorganisms, leading to an increase in CO_2 emissions from the soil[2]. Therefore, the thermal and chemical stability of char is crucial for effective soil carbon sequestration. Thermal stability is commonly characterized by the recalcitrance index (R_{50})[3], with higher R_{50} values indicating lower degradation rates and higher durability of char in environments with abiotic and biotic factors[4]. Aromatic moieties and a lower H/C ratio enhance the thermal stability of char[5,6]. Chemical stability is employed to simulate the natural oxidation process of char in the environment[7] and is defined by the rate of carbon loss following oxidation, with a lower carbon loss rate indicating greater chemical stability. Multiple factors influence the chemical stability of char, including the O/C and H/C atomic ratios and aromatic carbon content. As the O/C and H/C atomic ratios decrease and the aromatic carbon content increases, the chemical stability of char improves[6,8]. The specific surface area (SSA) also greatly influences the chemical stability, with a larger specific surface area leading to decreased chemical stability[9].

Hydrothermal carbonization involves the direct conversion from biomass to hydrochar in a subcritical state. Compared with pyrolysis, hydrothermal carbonization is not limited by the moisture content of biomass, eliminating the need for pre-drying and reducing energy consumption when processing biomass with high moisture content[10]. Compared with pyrolytic biochar, hydrochar has a lower aromatic content and is generally considered to be less stable[11,12]. Subcritical water has a relatively high solubility for hydrophobic organic compounds (HOCs). When hydrochar is prepared from plant aerial parts, such as palm leaves, the cuticle covering their surface dissolves and subsequently reprecipitates, forming a hydrophobic coating on the surface of hydrochar[13]. When there is a significant difference between the properties of the hydrophobic coating and the bulk hydrochar, the hydrophobic coating can greatly affect the stability of the hydrochar. For example, when calcium-rich invasive plants are used as feedstock, a calcium oxalate coating forms on the surface of hydrochar. The coating's barrier effect enhances the thermal and chemical stability of the hydrochar[14].

Because the cuticle includes cutin and waxes and has a complex composition, its content and composition vary across plant species, tissues, and organs[15]. The characteristics of a hydrophobic coating may vary due to the distinct properties of the cuticle. Leaves are the plant organs with the highest number of cuticles, and the surfaces of corn leaves, lotus leaves, palm leaves, and pine needles are all covered with cuticles. Our previous study demonstrated that hydrochar derived from palm leaves at 260 °C can form a hydrophobic coating on its surface[13], yet that work was limited to a single plant species and addressed only the coating's effects on specific surface area and oxygen-containing functional groups, without considering its implications for stability. The present study therefore expands the feedstock range to four distinct plant leaves—palm, corn, lotus, and pine—to compare the variations in hydrophobic coating properties among them, and more importantly, to investigate how these coating differences regulate the thermal and chemical stability of the resulting hydrochars. To this end, this study aimed to: (i) characterize the composition of the hydrophobic coating extracted from hydrochars derived from palm leaves, corn leaves, lotus leaves, and pine needles; (ii) analyze the physicochemical properties of hydrochars before and after removing the hydrophobic coating; (iii) assess the thermal and chemical stability of hydrochars before and after removing the hydrophobic coating; and (iv) elucidate the stabilization mechanism of hydrochar in relation to its physicochemical properties affected by the hydrophobic coating. The results of this study provide theoretical support for expanding the applications of hydrochar for soil carbon sequestration.

Materials and methods

Production of hydrochar

Biomass (corn leaves, lotus leaves, and pine needles) was collected from a village in Chongqing, China. The collected biomass was washed with tap water and dried in an oven (DHG-9240A, Shanghai Jing Hong Laboratory Instrument Co., Shanghai, China) at 60 °C before being

ground into powder using a planetary ball mill (model QM-3SP4, Nanjing Nanda Instrument Co., Nanjing, China) and passed through a 0.15-mm mesh sieve. The sieved material was used as raw material to prepare hydrochar and labeled as CL, LL, and PN for corn leaves, lotus leaves, and pine needles, respectively. Hydrothermal carbonization experiments were carried out in a magnetically stirred miniature high-pressure reactor (WCGF-200 mL, Xi'an Taikang Biotechnology Co., Shaanxi, China). A mixture of 10 g biomass and 90 mL deionized water was placed into the 200 mL stainless steel reactor. The reactor was then heated using an external resistance heater, with its temperature monitored by a thermocouple inserted into the reactor. The reaction was maintained at 260 °C for 5 h. Upon completion, the heater was turned off, and the stainless steel reactor was removed and allowed to cool naturally to room temperature. A vacuum filter device was used to separate the solid (hydrochar) and liquid in the hydrothermal carbonization products through a Buchner funnel. The filtered solid was mixed with 450 mL of deionized water, and the residue on the surface of the hydrochar was washed and then filtered. The above procedure was repeated more than five times to minimize residue in the liquid-phase product until the pH of the filtrate was stable. The solid hydrochar was frozen in a −50 °C freezer (DW-86L80, Zhejiang Jiesheng Low-Temp Equipment Co., Huzhou, China) and dried in a vacuum freeze-dryer (model LGJ-12, Huayu Xiongdi, Zhengzhou, China) with a cold trap temperature lower than −56 °C and vacuum of less than 10 Pa. The dried hydrochar was passed through a 0.15-mm mesh sieve and stored in a sealed bag until future analysis. Hydrochar prepared from corn leaves, lotus leaves, and pine needles was labeled as CL-H, LL-H, and PN-H, respectively. The previously prepared palm leaves and palm leaf hydrochar were labeled as PL and PL-H, respectively. Previous studies have shown that cellulose hydrochar does not form a hydrophobic coating[13]. Therefore, in this study, cellulose hydrochar was used as a control, and cellulose and cellulose hydrochar were labeled as CE and CE-H, respectively. The basic physicochemical data of PL-H and CE-H were cited from our published work[13], while all stability-related data and contact angle results in this study were newly obtained through independent experiments.

In situ characterization of the hydrophobic coating

The formation of the hydrophobic coating was characterized *in situ* using X-ray photoelectron spectroscopy (XPS) in conjunction with an argon ion etching technique. By controlling the etching time, the samples were progressively exposed to different depths (35, 70, 105, 150, 200, and 300 nm), allowing for an examination of their internal structure. The XPS analysis employed Al Kα X-rays as the excitation source, and by analyzing the intensity of the characteristic peaks of C, O, and N at various depths, the atomic ratios of these elements were calculated.

Hydrophobic coating extraction and composition identification

During the hydrothermal carbonization process, the polarity of water decreased, leading to a reduction in its dielectric constant. At 200 °C, the dielectric constant of water is comparable to that of methanol, while at 300 °C, it resembles that of acetone. To ensure the extraction of the hydrophobic coating, acetone was used. The extraction experiment was carried out in 40-mL vials with Teflon-lined screwcaps, in which 0.15 g hydrochar was added first, followed by 30 mL acetone according to a 200:1 mL g^{-1} liquid-solid ratio. The vial was shaken at 120 r min^{-1} for 24 h at 25 ± 0.5 °C in a shaker incubator (model ZQWY-220ES, Shanghai Zhichu Instrument Co., Shanghai, China) and then centrifuged at 2,500 r min^{-1} for 20 min using a DD5 centrifuge (Hunan Herexi Instrument and Equipment Co., Changsha, China). The supernatant was the extraction product, while the solid residue constituted the hydrochar after acetone extraction.

The solid was dried in an oven (DHG-9240A, Shanghai Jing Hong Laboratory Instrument Co., Shanghai, China) at 60 °C, weighed, ground, passed through a 0.15-mm mesh sieve, and then stored until further analysis. The mass loss rate of hydrochar was calculated based on the mass difference before and after acetone extraction. After acetone extraction, the hydrochar samples obtained from CE-H, CL-H, LL-H, PL-H, and PN-H were labeled as CE-H-ex, CL-H-ex, LL-H-ex, PL-H-ex, and PN-H-ex, respectively.

The chemical compositions of the extraction products were determined by gas chromatography–mass spectrometry (GC–MS). Filtration and derivatization were required before testing. A nylon syringe filter (0.45 μm pore size) was used to filter the extraction product. A 1 mL aliquot of the filtered extract was then transferred to a 2.5 mL vial with a Teflon-lined screwcap and evaporated to dryness under a nitrogen stream. Anhydrous pyridine (100 μL) and BSTFA-TMCS (100 μL) were added to the vial, which was then wrapped in aluminum foil and heated in an oven at 80 °C for 2 h. After naturally cooling to room temperature, the vial was placed in a refrigerator (BCD-521WDPW, Haier, Qingdao, China) at 4 °C for 24 h.

The composition of the derived extraction product was determined using a 7890A GC system with a 5975C quadrupole mass-selective detector (Agilent, Santa Clara, California, USA). The injection volume was 1 μL with a split ratio of 20:1. High-purity helium was used as the carrier gas with a flow rate of 1.5 mL min^{-1}. The heating program was as follows: an initial hold at 50 °C for 2 min, followed by heating at a rate of 5 °C min^{-1} to 150 °C, where it was held for 5 min. The temperature was then increased at the same rate to 200 °C and held for 5 min, followed by further heating to 250 °C with another 5 min hold. Finally, the temperature was raised to 300 °C at 5 °C min^{-1} and maintained for 5 min. The whole heating process took 72 min. The ionization mode was electron-impact ionization (EI) with an electron energy of 70 eV, inlet temperature of 280 °C, transfer line temperature of 280 °C, ion source temperature of 220 °C, quadrupole temperature of 150 °C, and scanning range of 10–500 amu. The detected components were searched in the National Institute of Standards and Technology (United States Department of Commerce) database (www.nist.gov/srd/nist-standard-reference-database-1a). The percentage of each component was calculated by the area normalization method[6].

Characterization of physicochemical properties of hydrochar

The C, H, N, O, and S contents of hydrochar samples were determined using an elemental analyzer (Vario MicroCube, Elementar Company, Germany). The crystalline structure of the hydrochar was determined by a SmartLab3 XRD (Rigaku, Tokyo, Japan). The surface morphology of the hydrochar was observed via a GeminiSEM 300 field emission scanning electron microscope (Zeiss, Munich, Germany). Contact angles were determined with an LSA100 goniometer (LAUDA Scientific, Germany) via static water droplet measurement to evaluate the surface hydrophobicity of hydrochar samples. The surface functional groups of the hydrochar were determined using FTIR spectroscopy (iS50 FT-IR, Thermo Fisher Scientific, USA), and the Brunauer–Emmett–Teller (BET) surface area was determined using a surface area analyzer (Micromeritics, Norcross, Georgia, USA). The carbon structure of the hydrochar was determined using a

https://doi.org/10.48130/ebp-0026-0012

solid-state ^{13}C nuclear magnetic resonance (NMR) spectrometer (JNM-ECZ600R, JEOL, Tokyo, Japan) with a resonance frequency of 150.91 MHz, a magic angle spinning frequency of 8 kHz, a contact time of 27.2 ms, and a pulse delay of 3.0 s.

Determination of hydrochar thermal stability

The thermogravimetric (TG) curves of hydrochar samples were obtained by a simultaneous thermal analyzer (DSC/DTA-TG) (STA 449 F5 Jupiter®, NETZSCH, Germany). Samples (8–10 mg) were heated from 25 to 1,000 °C under an air atmosphere at a rate of 10 °C min^{-1}. The TG curves were corrected by deducting the ash content from the samples. The thermal stability of the hydrochar was evaluated using the recalcitrance index, R_{50}, proposed by Harvey et al.[3], which was calculated as:

$$R_{50} = T_{50x}/T_{50\ graphite} \quad (1)$$

where, T_{50x} and $T_{50\ graphite}$ are the temperatures corresponding to 50% mass loss in the corrected TG curves for the sample and graphite, respectively. According to Harvey et al.[3], $T_{50\ graphite}$ is 886 °C.

The TG curves were further processed by model-fitting kinetic analysis to quantify the thermal-decomposition behavior of the hydrochar. The Coats–Redfern integral method was applied because it allows the activation energy (E) and the pre-exponential factor (A) to be extracted from a single-heating-rate experiment[16]. The working equation is:

$$\ln[g(\alpha)/T^2] = \ln(AR/\beta E) - E/(RT) \quad (2)$$

where, $\alpha = (m_0 - m_t)/(m_0 - m_\infty)$ denotes the fractional conversion; m_0, m_t, and m_∞ are the initial, instantaneous, and final sample masses (mg); β is the linear heating rate (K min^{-1}); R is the universal gas constant (8.314 J mol^{-1} K^{-1}); T is the absolute temperature (K); and $g(\alpha)$ is the integral form of the reaction model. Specifically, E represents the activation energy (J mol^{-1}), and A refers to the pre-exponential factor (min^{-1}). The most commonly used $g(\alpha)$ expressions are listed in Supplementary Table S1.

The kinetic analysis proceeded as follows. First, α was calculated from the TG curve at 10 K min^{-1} intervals. Referring to previous literature[17], data points within the conversion range α = 0.2–0.8 were adopted for subsequent fitting. For each $g(\alpha)$ model, $\ln[g(\alpha)/T^2]$ was plotted against $1/T$ and the data were fitted by ordinary least-squares regression. The model yielding the highest coefficient of determination (R^2) was taken as the statistically most probable reaction mechanism. Subsequently, E and A were obtained from the slope k and intercept b of the best-fit line via:

$$E = -kR \quad (3)$$

$$A = (\beta E/R)\exp(b) \quad (4)$$

To eliminate manual calculation deviations and ensure the accuracy and reproducibility of kinetic parameter results, all the above computational procedures were programmatically implemented via Python on the PyCharm platform, and the complete calculation code is provided in the Supplementary Text 1.

Measurement of chemical stability of hydrochar

The chemical stability of hydrochar was determined using the potassium dichromate ($K_2Cr_2O_7$) oxidation method[9]. The hydrochar sample containing 0.04 g of organic carbon was placed into 40 mL vials with Teflon-lined screwcaps, and 30 mL of 0.1 M $K_2Cr_2O_7$/2 M H_2SO_4 solution was added. All experiments were conducted in triplicate for repeatability. A blank control without a hydrochar sample was treated under the same conditions for blank correction. Theoretical calculations indicated that even with complete oxidation of the organic carbon in hydrochar, the residual Cr(VI) in the oxidation solution comprised 26.0% of the initial dosage.

The vials were shaken at 120 rpm for 60 h at 55 °C in a shaker incubator (model ZQWY-220ES, Shanghai Zhichu Instrument Co., Shanghai, China). During the reaction, the vials were opened multiple times to release the gas formed. After the reaction, the vials were centrifuged at 2,500 r min^{-1} for 10 min using a DD5 centrifuge (Hunan Herexi Instrument and Equipment Co., Changsha, China), and the supernatant was filtered through 0.45 μm Millipore filters. The Cr(VI) concentration in the filtrate was detected using the diphenyl-carbazide spectrophotometric method at 540 nm. A calibration curve was established with a series of Cr(VI) standard solutions (0–0.4 mg L^{-1}) for quantitative analysis, and all test results were corrected with the blank control. The blank test verified that the Cr(VI) concentration remained constant in the blank group before and after the reaction, confirming no spontaneous reduction or loss of Cr(VI) in the absence of hydrochar, which guaranteed the accuracy of experimental data.

Carbon loss was determined by the consumption of Cr(VI) based on the following chemical equation:

$$2K_2Cr_2O_7 + 3C + 8H_2SO_4 \rightarrow 2K_2SO_4 + 2Cr_2(SO_4)_3 + 3CO_2\uparrow + 8H_2O$$

The carbon loss rate was calculated based on the ratio of the amount of carbon lost to that of organic carbon in hydrochar. Combined with the redox stoichiometric relationship and the consumed molar amount of Cr(VI), all calculation parameters were integrated into a unified formula. The mathematical expression for the carbon loss rate is presented as follows:

$$L(\mathrm{C}) = \frac{3 \times (C_{initial} - C_{residual}) \times V \times M(\mathrm{C})}{4 \times M(\mathrm{C_r}) \times m(\mathrm{C})_{initial}} \times 100\% \quad (5)$$

where, L(C) is the carbon loss rate (%), $C_{initial}$ and $C_{residual}$ are the initial and residual mass concentrations of C_r(VI) (g L^{-1}) in the reaction solution, V is the volume of the added oxidizing solution (L), $M(C_r)$ is the molar mass of chromium (52.00 g mol^{-1}), M(C) is the molar mass of carbon (12.01 g mol^{-1}), and $m(C)_{initial}$ is the initial organic carbon mass of hydrochar (0.04 g).

The solid residues in the bottom of vials were frozen at −50 °C in a freezer (DW-86L80, Zhejiang Jiesheng Low-Temp Equipment Co., Huzhou, China) for a duration of 12 h. Following freezing, the samples were transferred to a vacuum freeze-dryer (model LGJ-12, Huayu Xiongdi, Zhengzhou, China) and dried for 24 h to obtain the dried solid residues. The solid residues obtained from the chemical oxidation of leaf-derived hydrochars were designated as CL-H-RS, LL-H-RS, PL-H-RS, and PN-H-RS, respectively.

Statistical analysis

One-way analysis of variance (ANOVA) was used to test the significance of differences between hydrochars obtained from different biomass sources ($p < 0.05$ was considered significant). Least Significant Difference (LSD) was used for multiple comparisons. A t-test was used to determine the significance of differences before and after acetone extraction. Pearson correlation was used for correlation analysis. All statistical analyses were performed using SPSS 20.0 (IBM, Armonk, NY, USA). Principal component analysis (PCA) was performed using CANOCO v5.0 (Microcomputer Power, Ithaca, NY, USA).

Results and discussion

Hydrophobic alkyl carbon components of the cuticle affect the properties of the hydrophobic coating

The (O + N)/C atomic ratio increased with increasing depths of leaf-derived hydrochar (Supplementary Fig. S1). This ratio at the same depth of the leaf-derived hydrochar was consistently lower than that of the raw biomass, preliminarily suggesting the potential formation of a hydrophobic surface layer on leaf-derived hydrochar. To substantiate this inference, we conducted direct morphological observations and static water contact angle measurements on hydrochar before and after acetone treatment. The pristine leaf-derived hydrochars exhibited intact and relatively smooth surface morphology, while distinct porous structures could be clearly observed after acetone treatment (Supplementary Fig. S2). The exposure of originally blocked pores strongly demonstrates the effective removal of the surface covering layer, and the relevant increase in specific surface area will be systematically discussed in the subsequent section. Contact angle tests further complement the structural evidence: the cellulose hydrochar (CE-H) showed a low contact angle of 59.3°, while the four leaf-derived hydrochars exhibited much higher contact angles ranging from 127.0° to 149.1° (Supplementary Fig. S3), verifying the strong surface hydrophobicity of pristine leaf-derived hydrochar. Notably, the contact angle showed no obvious change after extraction, which could be well explained by the Cassie–Baxter principle[18]. The removal of surface hydrophobic components weakened surface chemical hydrophobicity and tended to decrease the contact angle[19], whereas the newly exposed pores increased surface roughness and improved physical hydrophobicity via air entrapment, which tended to increase the contact angle. The counterbalance between these two opposite effects resulted in stable macroscopic wettability, further confirming the obvious surface structural alteration induced by acetone treatment. Combined with the above morphological and wettability results, it can be fully confirmed that a hydrophobic coating is formed on the surface of leaf-derived hydrochar, and acetone extraction can effectively remove this surface hydrophobic covering layer.

The hydrochar samples exhibited extraction yields of 13.70% (CE-H), 32.46% (CL-H), 29.48% (LL-H), 29.57% (PL-H), and 28.01% (PN-H). Despite the comparable coating loadings among the four leaf-derived hydrochars, their coating compositions differed markedly (Table 1). To trace this compositional divergence, we analyzed the acetone-extractable fractions and surface wettability of the raw leaves. Lotus leaves showed a high contact angle of 133.7°, consistent with their abundant extractable wax marker nonacosane-4,10-diol[20], which accounted for 62.63% of total hydrophobic organic compounds (HOCs). In contrast, the raw CL, PL, and PN leaves exhibited much lower contact angles and HOC contents of only 8.21%–12.63%, indicating negligible wax abundance. Given that cuticular waxes are structurally stable long-chain aliphatics while cutin is an ester-rich polyester susceptible to hydrothermal hydrolysis[21,22], these inherent differences govern the final hydrochar coating origins. Accordingly, during 260 °C carbonization, the robust wax skeletons of lotus leaves were largely preserved[23], resulting in LL-H coatings dominated by nonacosane-4,10-diol. Conversely, the ester-rich cutin in CL, PL, and PN underwent extensive depolymerization, releasing characteristic C16 monomers (palmitic acid and 16-hydroxypalmitic acid) that constituted the hydrophobic coatings on CL-H, PL-H, and PN-H. Collectively, these results confirmed that the hydrophobic coating of LL-H derived mainly from intrinsic leaf wax, while that of CL-H, PL-H, and PN-H originated from cutin degradation products.

Generally, a larger Log*P* value indicates a more hydrophobic organic compound, where *P* represents the octanol–water partition coefficient[24]. All Log*P* values used in this study were retrieved from the PubChem database. Experimentally measured Log*P* values were preferentially adopted when available, and the database-built semi-empirical XlogP3 values were used for compounds without

Table 1 Hydrophobic organic compounds identified in the extraction products of hydrochar derived from different biomass

Number	Compound name	Molecular formula	Log*P*[a]	Peak area percentage (%)				
				CE-H	CL-H	LL-H	PL-H	PN-H
1	Hexylmalonic acid	$C_9H_{16}O_4$	2.1	–[b]	2.21	–	–	–
2	3,5-Dimethylphenol	$C_8H_{10}O$	2.4	–	1.05	–	–	–
3	12-Hydroxydodecanoic acid	$C_{12}H_{24}O_3$	3.6	–	–	–	–	4.08
4	14-Hydroxymyristic acid	$C_{14}H_{28}O_3$	3.7	–	–	–	–	7.76
5	Dehydrodiisoeugenol	$C_{20}H_{22}O_4$	4.4	–	–	–	–	1.60
6	Dodecanoic acid	$C_{12}H_{24}O_2$	4.6	–	1.49	–	–	–
7	16-Hydroxy-9-Hexadecenoic acid	$C_{16}H_{30}O_3$	4.6	–	–	3.00	–	–
8	16-Hydroxypalmitic acid	$C_{16}H_{32}O_3$	4.8	–	1.53	–	–	36.73
9	Dehydroabietic acid	$C_{20}H_{28}O_2$	5.6	–	1.07	–	–	9.10
10	Myristic acid	$C_{14}H_{28}O_2$	6.11	–	1.36	–	1.32	–
11	Oleic acid	$C_{18}H_{34}O_2$	6.5	–	1.33	–	–	1.46
12	Ergosterol peroxide	$C_{28}H_{44}O_3$	6.7	–	1.60	–	–	–
13	Palmitic acid	$C_{16}H_{32}O_2$	7.17	–	17.62	13.86	24.07	5.64
14	Stearic acid	$C_{18}H_{36}O_2$	7.4	–	4.17	1.45	8.31	–
15	3-Methoxycholest-7-en-6-ol	$C_{28}H_{48}O_2$	7.7	–	1.68	–	–	–
16	β-Sitosterol	$C_{29}H_{50}O$	9.3	–	7.69	11.66	4.03	4.65
17	Nonacosane-4,10-diol	$C_{29}H_{60}O_2$	12.1	–	–	20.78	–	–
18	alpha-Tocopherol	$C_{29}H_{50}O_2$	12.2	–	–	–	2.74	–
19	Nonacosan-10-ol	$C_{29}H_{60}O$	14	–	–	14.66	–	2.40
20	17-Pentatriacontene	$C_{35}H_{70}$	18.2	–	–	1.02	–	–

Note: [a] *P* is the octanol-water partition coefficient; [b] – means non-detected. All data are derived from single GC–MS measurements without replicates. Log*P* values were retrieved from the PubChem database. CE-H, CL-H, LL-H, PL-H, and PN-H represent hydrochar prepared from cellulose, corn leaves, lotus leaves, palm leaves, and pine needles, respectively.

https://doi.org/10.48130/ebp-0026-0012

experimental data. The Log*P* values of palmitic acid, 16-hydroxypalmitic acid, and nonacosane-4,10-diol varied greatly, with nonacosane-4,10-diol having the highest value of 12.1. Due to the different main compositions of HOCs in different hydrochar samples, it is essential to consider both the peak area percentage and the Log*P* value of each HOC when investigating the overall properties of the hydrophobic coating. This study introduced the concept of hydrophobic intensity of hydrophobic coating, which was defined as the sum of the products of the peak area percentage and the Log*P* value for all HOCs within a hydrophobic coating. The mathematical expression for this parameter was:

$$I = \sum_{i=1}^{n} F_i S_i \tag{6}$$

where, I is the hydrophobic intensity of the hydrophobic coating; F_i is the Log*P* value of the *i*-th HOC; S_i is the relative peak area percentage of the *i*-th HOC obtained from GC–MS total ion chromatograms (%).

It is noteworthy that the GC–MS-derived relative peak area percentage is used for semi-quantitative component analysis in this study. Due to varying EI detector response factors among organic compounds, peak area proportions cannot precisely represent molar or mass fractions. However, this method is commonly used for comparative analysis of organic component abundance in biomass-derived samples and is reliable for evaluating the relative hydrophobic contribution of individual HOCs in this work. The *I* values of CL-H, LL-H, PL-H, and PN-H were 2.97, 7.08, 3.13, and 4.05, respectively, with LL-H hydrophobic coating exhibiting the largest *I* value. Meanwhile, the *I* value of CE-H was zero. Correlation analysis between *I* values and contact angles was performed to verify the index. However, no significant correlation was observed. This is because the hydrophobic intensity index only reflects the intrinsic molecular hydrophobicity of organic components, while the contact angle represents the overall macroscopic wettability of materials affected by multiple factors beyond organic chemical properties. Thus, this empirical index was only suitable for qualitatively evaluating the relative hydrophobic contribution of organic coating components and cannot fully characterize the practical macroscopic hydrophobic performance of hydrochar materials. The difference in hydrophobic intensity among these samples was inherently determined by the distinct biochemical compositions of raw plant cuticles: the wax-dominated coating of LL-H contained abundant high-Log*P* components, whereas the cutin-based coatings of the other three samples relied on less hydrophobic substances.

Although the hydrophobic coating of CL-H and PL-H had the same main composition, they showed slight differences in their hydrophobic intensity. Palmitic acid, a saturated fatty acid, can form a crystalline structure by assembling into dimers through O–H…O hydrogen bonding under suitable conditions[25,26]. The XRD patterns showed that PL-H contained strong diffraction peaks of palmitic acid crystals, while CL-H did not (Fig. 1a, b). This indicated that the palmitic acid arrangement in PL-H was ordered, forming a crystalline coating, while the palmitic acid arrangement in CL-H was more disordered. This difference can be attributed to the presence of other HOCs, such as β-sitosterol, which serve as impurities and inhibit the crystallization of palmitic acid during the formation of the hydrophobic coating[27]. Impurities affect the crystallization process in a concentration-dependent manner, where higher concentrations are more likely to inhibit crystal formation[28,29]. Analyzing the ratio of the total peak percentage of non-palmitic acid HOCs to the peak area of palmitic acid within the hydrophobic coating showed that the ratios of CL-H and PL-H were 1.43 and 0.68, respectively. This indicated a higher content of other HOCs, excluding palmitic acid, in the CL-H hydrophobic coating, which significantly inhibited the crystallization of palmitic acid.

Combining the elemental composition of hydrochar before and after acetone extraction (Table 2), we calculated the mass loss of hydrochar and of each element within the hydrochar. The ratio of the mass loss of each element to the overall mass loss of hydrochar represented the relative content of elements in the extraction product, which was mathematically expressed as:

$$\gamma = \frac{MC_0 - (100\%\text{-}\eta)MC_1}{M\eta} = \frac{C_0 - (100\%\text{-}\eta)C_1}{\eta} \tag{7}$$

where, γ is the relative content of an element in the extraction product (%); M is the mass (g) of the hydrochar before extraction; η is the mass loss rate of the hydrochar after extraction (%); C_0 is the relative content of an element in hydrochar before extraction (%); C_1 is the relative content of an element in the hydrochar after extraction (%).

Based on the relative contents of C, H, and O elements in the extraction products, the H/C atomic ratio and O/C atomic ratio were calculated (Supplementary Fig. S4). Compared with the CE-H extraction product, the H/C atomic ratios of the extraction products from leaf-derived hydrochar increased by 48.80% to 81.86%, while their O/C atomic ratios decreased by 28.98% to 68.48%. Compared with the bulk elemental composition of hydrochar, the H/C atomic ratios of the leaf-derived hydrochar extraction products increased by 13.66%–24.57%, and the O/C atomic ratios decreased by 26.49%–60.72%. These results indicated that the high H/C atom ratio and low O/C atom ratio of the hydrophobic coating were consistent with those of the hydrophobic alkyl carbon. Moreover, the H/C atomic ratio of the LL-H extraction product was the highest, and that of the CL-H extraction product was the lowest. The H/C atomic ratio of the extraction product was significantly positively correlated with the *I* value of the hydrophobic coating (n = 5, r = 0.884, p = 0.047). It should be noted that the correlation analyses were based on a small sample set (n = 5), making the results sensitive to individual variations. Thus, the observed trends are primarily applicable to the specific leaf-derived hydrochars studied, and extension to other biomass types requires further validation. Nonetheless, the high correlation coefficients and statistically significant *p*-values, alongside diverse characterization data, demonstrated that the conclusions drawn in this work were valid and reliable.

After removing the hydrophobic coating by acetone extraction, the C and H contents in leaf-derived hydrochar were significantly lower. The H/C atomic ratios of leaf-derived hydrochar were all reduced, with the largest reduction in LL-H-ex (15.5%). The magnitude of the reduction in the H/C atomic ratio was significantly positively correlated with the *I* value of the hydrophobic coating (n = 5, r = 0.927, p = 0.024). The C–H stretching vibrational peaks (2,800–3,000 cm^{-1}) of methyl and methylene groups were substantially weaker after acetone extraction (Fig. 1c, d). Based on the solid-state ^{13}C-NMR spectral analysis, the alkyl carbon content in leaf-derived hydrochars decreased by 15.27%–23.44% after acetone extraction (Table 3). Combined with the decrease in the H/C atomic ratio, this further indicated that acetone extraction removed a large amount of alkyl carbon. Thus, the composition and properties of the hydrophobic coating were mainly regulated by the fraction of hydrophobic alkyl carbon in the cuticle.

The physicochemical properties of hydrochar were altered by hydrophobic alkyl carbon coatings

Our previous work showed that removing a hydrophobic coating significantly increased the SSA and polarity of hydrochar[13]. Here, we

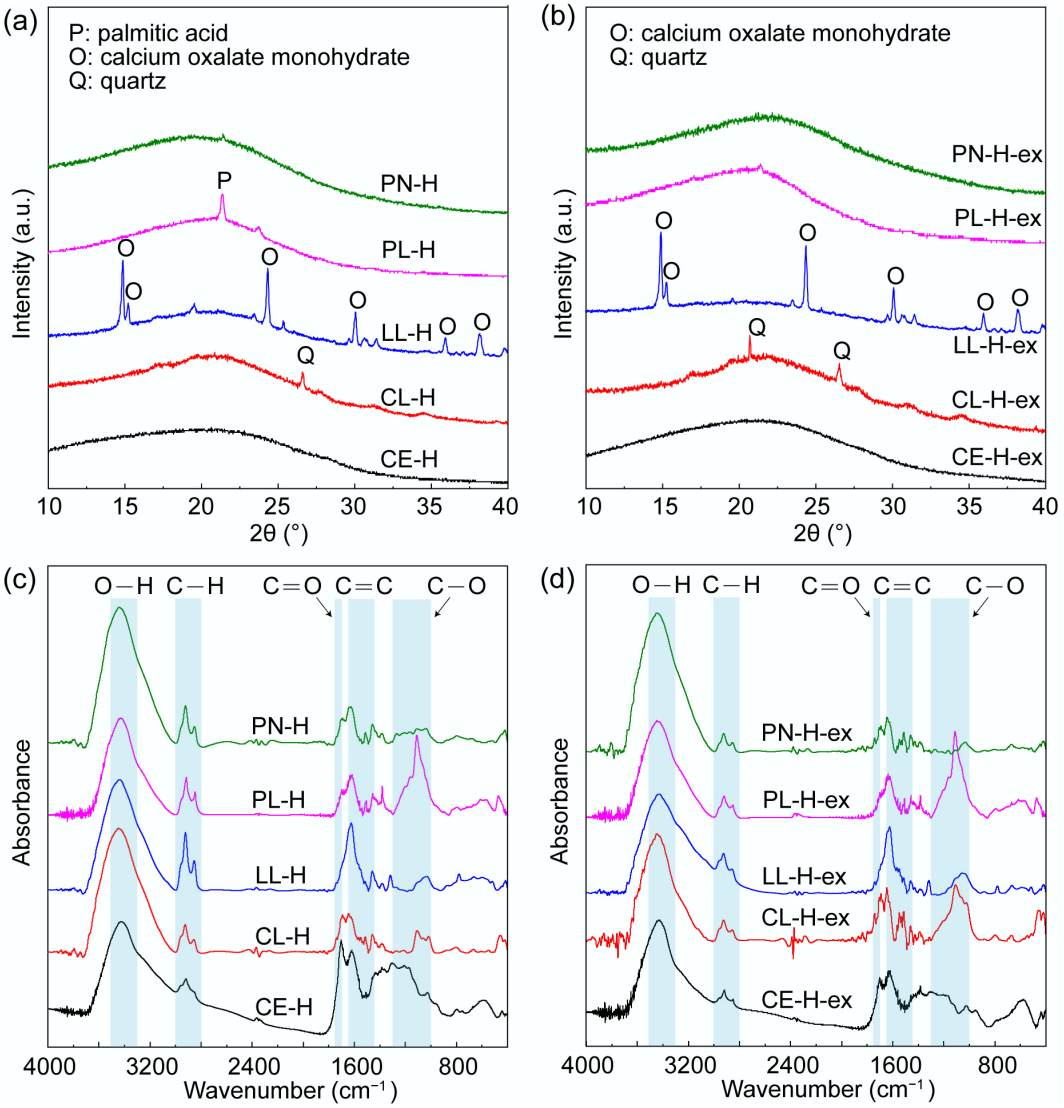

Fig. 1 (**a**), (**b**) XRD patterns and (**c**), (**d**) FTIR spectra of different hydrochar samples before (left column) and after (right column) acetone extraction. Abbreviation definitions: CE-H, CL-H, LL-H, PL-H, and PN-H represent unextracted hydrochar derived from cellulose, corn leaves, lotus leaves, palm leaves, and pine needles, respectively; CE-H-ex, CL-H-ex, LL-H-ex, PL-H-ex, and PN-H-ex correspond to acetone-extracted hydrochar samples.

further investigated its effect on the physicochemical properties of four kinds of leaf-derived hydrochar (Table 2). The polarity of all leaf-derived hydrochars increased after extraction, as shown by their higher O/C ratios. Thus, the presence of hydrophobic coatings reduced hydrochar polarity, which was consistent with our previous results. Other studies have shown that low H/C and O/C atomic ratios indicated a higher stability of hydrochar[30]. The removal of hydrophobic coating decreased the H/C atomic ratio and increased the O/C atomic ratio. This divergence hindered the understanding of the effect of the hydrophobic coating on hydrochar's stability. Notably, the H/C and O/C ratios of the hydrophobic coating differed markedly from those of the bulk hydrochar, highlighting the heterogeneity of leaf-derived hydrochar. Therefore, assessing the stability of hydrochar solely based on its bulk elemental atom ratio is not reasonable; the hydrophobic coating on its surface must also be taken into account.

It has been reported that the SSA of char also greatly affects its chemical stability[9,31]. After acetone extraction, the SSA of all leaf-derived hydrochars increased due to the removal of a hydrophobic coating that blocked their pores (Fig. 2a). This conclusion was further supported by SEM characterization. As shown in Supplementary Fig. S2, the surface pores of the four leaf-derived hydrochars were covered by the coating before extraction and clearly exposed after acetone treatment. Notably, among the four kinds of leaf-derived hydrochars, CL-H and PL-H had the largest and smallest SSA, respectively. The SSA of CL-H was 123.5% higher than that of PL-H due to the crystalline nature of the hydrophobic coating of PL-H. Crystalline coatings are typically dense and uniform, effectively sealing pores[32,33]. After removing the hydrophobic coating, the SSA of CL-H increased by 70.78%, while that of PL-H increased by 323.8%, significantly reducing the difference in SSA.

After acetone extraction, the aromatic carbon content of leaf-derived hydrochar increased by 2.82%–15.62%, while its aromaticity rose by 8.49%–13.54% (Table 3). These results indicated an obvious reduction in alkyl carbon content following extraction, confirming that the interior of the hydrochar, previously covered by a hydrophobic coating, contained a higher proportion of aromatic carbon. The leaf-derived hydrochars before extraction all contained high alkyl carbon contents, which is inconsistent with previous

https://doi.org/10.48130/ebp-0026-0012

Table 2 Elemental composition of hydrochar samples before and after acetone extraction

Sample	C (%)	H (%)	O (%)	N (%)	S (%)	H/C	O/C
CE	42.07 ± 0.24	6.41 ± 0.01	52.48 ± 2.32	–[I]	–	1.83	0.94
CE-H	70.16 ± 0.40a[II]	4.76 ± 0.05a	25.54 ± 0.41b	–	–	0.81	0.27
CE-H-ex	68.04 ± 0.92a	4.65 ± 0.07a	26.86 ± 0.15a	–	–	0.82	0.30
CL	41.40 ± 0.35	5.59 ± 0.08	28.59 ± 0.47	1.59 ± 0.01	0.13 ± 0.01	1.62	0.52
CL-H	62.90 ± 1.15a	5.35 ± 0.11a	9.74 ± 0.49a	2.58 ± 0.05a	0.17 ± 0.01a	1.02	0.12
CL-H-ex	55.88 ± 0.77b	4.32 ± 0.10b	11.99 ± 2.47a	2.61 ± 0.04a	0.18 ± 0.01a	0.93	0.16
LL	44.53 ± 0.83	5.78 ± 0.11	30.49 ± 0.14	3.85 ± 0.07	0.21 ± 0.01	1.56	0.51
LL-H	63.76 ± 1.66a	6.05 ± 0.05a	14.10 ± 2.20a	3.41 ± 0.23a	0.08 ± 0.07a	1.14	0.17
LL-H-ex	58.48 ± 0.55b	4.80 ± 0.06b	17.22 ± 1.17a	3.60 ± 0.05a	0.15 ± 0.01a	0.99	0.22
PL	43.72 ± 0.81	6.13 ± 0.36	38.61 ± 0.87	1.62 ± 0.09	0.13 ± 0.08	1.68	0.66
PL-H	63.65 ± 0.93a	6.12 ± 0.26a	15.44 ± 0.37b	2.24 ± 0.04b	0.04 ± 0.02a	1.15	0.18
PL-H-ex	57.10 ± 0.83b	4.97 ± 0.21b	17.15 ± 0.49a	2.41 ± 0.05a	0.05 ± 0.04a	1.05	0.23
PN	49.72 ± 0.53	6.27 ± 0.07	36.20 ± 1.06	1.65 ± 0.01	0.11 ± 0.01	1.51	0.55
PN-H	74.14 ± 2.01a	6.14 ± 0.06a	14.82 ± 0.95a	2.28 ± 0.08a	0.08 ± 0.02	0.99	0.15
PN-H-ex	69.41 ± 0.80b	5.19 ± 0.07b	15.65 ± 0.85b	2.40 ± 0.03b	–	0.90	0.17

Note: data are presented as mean ± standard deviation, $n = 3$ parallel replicates. [I] – means non-detected; [II] a and b indicate a significant difference in the bulk elemental composition of hydrochar before and after acetone extraction, and the same letter means no significant difference. CE, CL, LL, PL, and PN denote raw cellulose, corn leaves, lotus leaves, palm leaves, and pine needles; CE-H, CL-H, LL-H, PL-H, and PN-H are the corresponding hydrochar samples; CE-H-ex, CL-H-ex, LL-H-ex, PL-H-ex, and PN-H-ex refer to acetone-extracted hydrochar samples.

Table 3 Carbon structure of hydrochar before and after acetone extraction determined by solid-state ^{13}C-NMR spectroscopy

Sample	Alkyl C/%	O–alkyl C/%	Aryl C/%	O–aryl C/%	Carboxyl C/%	Carbonyl C/%	Aromaticity/%
CE	0.00	100.00	0.00	0.00	0.00	0.00	0.00
CE-H	25.00	12.27	45.00	8.64	2.27	6.82	59.00
CE-H-ex	26.29	12.68	42.25	8.92	2.35	7.51	56.77
CL	10.54	79.33	5.17	0.05	4.91	0.00	5.49
CL-H	45.75	9.48	36.71	2.70	0.47	4.89	41.64
CL-H-ex	35.83	11.90	37.74	4.78	1.89	7.86	47.11
LL	21.63	59.60	6.90	1.79	10.08	0.00	9.66
LL-H	50.83	8.48	32.38	3.14	2.56	2.60	37.45
LL-H-ex	38.91	12.65	33.63	4.52	5.18	5.10	42.52
PL	13.98	66.82	7.99	3.38	7.83	0.00	12.33
PL-H	42.65	13.50	29.27	8.96	2.75	2.87	40.51
PL-H-ex	36.14	15.76	33.84	8.34	2.60	3.31	44.84
PN	12.37	67.25	12.07	3.41	4.83	0.07	16.28
PN-H	43.97	10.18	34.72	4.56	1.57	5.00	42.05
PN-H-ex	36.50	14.14	37.23	5.25	1.70	5.19	45.61

Note: all values originate from single measurements without replicates. Aromaticity (%) = 100 × (Aryl C + O-aryl C)/(Alkyl C + O-alkyl C + Aryl C + O-aryl C). Sample abbreviations are consistent with Table 2.

literature[34,35]. Hydrochar prepared at higher temperatures usually has a higher content of aromatic carbon. In this study, the highest carbonaceous component of cellulose-derived hydrochar was aromatic carbon. This difference is due to the formation of a hydrophobic coating on the surface of all leaf-derived hydrochars. Before the extraction, LL-H had the highest alkyl carbon content, which was 19.18% higher than the minimum (PL-H). There was a significant positive correlation between the alkyl carbon and the I value of hydrophobic coating ($n = 5$, $r = 0.903$, $p = 0.036$), which confirmed that hydrophobic alkyl carbon of the hydrophobic coating significantly affected properties of leaf-derived hydrochars. Studies have shown that the carbon structure of hydrochar is a key factor affecting its stability[36]. Thus, hydrophobic alkyl carbon coatings changed the properties and structure of hydrochar, which in turn altered its chemical stability.

Hydrophobic coating reduces activation energy and pre-exponential factor without changing hydrochar thermal stability

The recalcitrance index (R_{50}) of hydrochar before and after acetone extraction is shown in Fig. 2b. After acetone extraction, there was no significant change in the R_{50} values of CL-H, PL-H, and PN-H, except for an increase for LL-H, which indicated no significant change in the thermal stability of hydrochar after removing the hydrophobic coating. Thermal decomposition behaviors of hydrochars were analyzed using the Coats–Redfern kinetic model. The kinetic parameters of thermal decomposition are listed in Table 4, while the corresponding TG/DTG curves, fractional conversion α curves, and kinetic fitting plots of typical leaf-derived hydrochars (PL-H) before and after acetone extraction are displayed (Supplementary Fig. S5). Based on the above kinetic results, the E values of leaf-derived hydrochars exhibited a strong negative correlation with the I values of their hydrophobic coatings ($n = 5$, $r = -0.971$, $p = 0.006$). After acetone extraction, E values increased in all samples by 12.8% to 63.6%. Generally, a lower E value indicated a reduced energy barrier, which, in turn, facilitated the thermal decomposition[37].

These results demonstrate that hydrophobic coatings reduce the activation energy. During thermal decomposition, alkyl carbons are more reactive than aromatic carbons[38]; thus, reactions dominated by alkyl species are characterized by lower E. Given that hydrophobic coatings were predominantly alkyl-rich, their presence decreases the overall E of the hydrochars. Upon removal of these coatings, the

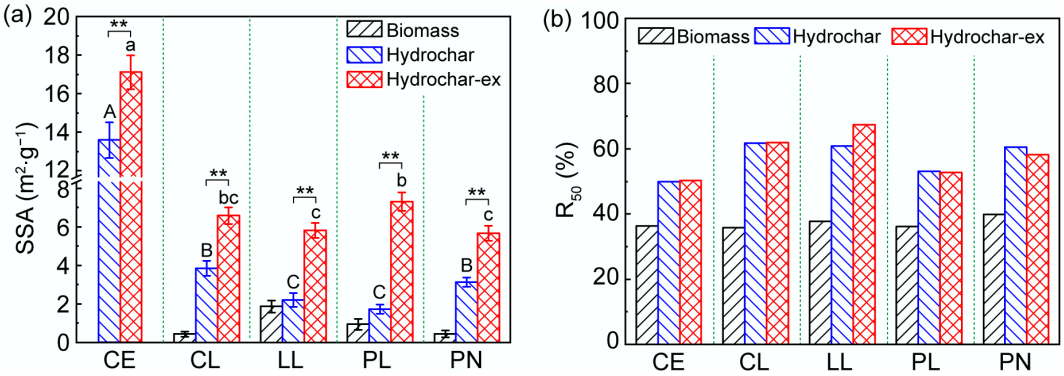

Fig. 2 (**a**) Specific surface area (SSA) of hydrochar derived from different biomass before and after acetone extraction. (**b**) Recalcitrance index (R_{50}) of hydrochar before and after acetone extraction. SSA = specific surface area; R_{50} = recalcitrance index. CE, CL, LL, PL, and PN represent raw cellulose, corn leaves, lotus leaves, palm leaves, and pine needle biomass, respectively; Hydrochar denotes unextracted hydrochar, and Hydrochar-ex denotes acetone-extracted hydrochar. (**A**)–(**C**) compare the SSA of different hydrochar samples before extraction, and (**a**)–(**c**) represent the comparison of SSA of different hydrochar after extraction. ** represents a significant difference ($p < 0.01$) in the SSA of hydrochar before and after extraction.

remaining aromatic framework exhibited greater thermal stability[39], increasing the energetic barrier and slowing the reaction.

The *A* value characterizes the frequency of molecular collisions occurring in the correct orientation for reaction[40]. *A* values below 10^9 s^{-1} signify surface-controlled kinetics, in which the reaction rate is governed by the SSA[41]. All leaf-derived hydrochars were below this threshold. After extraction, the SSA increased, and *A* rose correspondingly, thereby enhancing surface reactivity. This increase in *A* values offset the higher *E*, resulting in no significant change in the overall thermal stability of the hydrochars after the removal of hydrophobic alkyl carbon coatings.

Hydrophobic alkyl carbon coating determines the chemical stability of hydrochar

To investigate the effect of hydrophobic alkyl carbon coatings with different properties on the chemical stability of hydrochars, the carbon loss rates of hydrochars oxidized by $K_2Cr_2O_7$ before and after acetone extraction are shown in Fig. 3a. Before extraction, the carbon loss rates of leaf-derived hydrochars were markedly lower than those of CE-H, indicating that leaf-derived hydrochars exhibited greater chemical stability than CE-H. Principal component analysis (PCA) of the carbon loss rate and aromaticity, SSA, and *I* value of hydrophobic coating revealed a significant positive correlation between the carbon loss rate and aromaticity ($n = 5$, $r = 0.931$, $p = 0.021$) (Supplementary Fig. S6). This positive trend is primarily governed by the protective performance of the surface hydrophobic coating itself: higher aromaticity in the coating corresponds to poorer barrier properties, thereby accelerating the carbon loss. This intrinsic surface effect, often overlooked in previous studies, became a critical factor here. In contrast, Han et al.[42] reported a significant negative correlation between the carbon loss rate and aromaticity, attributing higher aromaticity to greater chemical stability. This discrepancy highlighted that the role of aromaticity in carbon stability was highly dependent on the specific material system—specifically, whether the surface coating's protective function is taken into account.

Table 4 Kinetic parameters for thermal decomposition of hydrochar before and after acetone extraction

Sample	Activation energy, *E* (J mol^{-1})	Pre-exponential factor, *A* (min^{-1})	$g(\alpha)$	Coefficient of determination, R^2
CE-H	57.51	347.88	$(1-\alpha)\ln(1-\alpha)+\alpha$	0.999
CE-H-ex	57.27	315.06	$(1-\alpha)\ln(1-\alpha)+\alpha$	0.999
CL-H	47.46	13.25	$(1-\alpha)\ln(1-\alpha)+\alpha$	0.992
CL-H-ex	55.83	595.50	$[(1-\alpha)^{-2}-1]/2$	0.981
LL-H	21.29	0.60	$-\ln(1-\alpha)$	0.987
LL-H-ex	33.43	8.47	$[(1-\alpha)^{-2}-1]/2$	0.978
PL-H	45.97	44.32	α^2	0.999
PL-H-ex	52.28	145.55	α^2	0.999
PN-H	43.87	13.71	α^2	0.986
PN-H-ex	48.77	23.82	$(1-\alpha)\ln(1-\alpha)+\alpha$	0.994

Sample abbreviations are defined in Table 2. α = fractional conversion; $g(\alpha)$ = integral form of the reaction model.

Compared with the hydrochars before oxidation, the H/C atomic ratios of oxidized hydrochars increased by 64.3% to 93.4% (Fig. 3b). Furthermore, the C–H stretching vibration peaks of alkyl carbon (2,850–2,925 cm^{-1}) showed significant enhancement (Fig. 3c). These results indicated a higher content of alkyl carbon in the oxidized hydrochars, confirming that the alkyl carbon in hydrochar possessed a strong resistance to chemical oxidation. To further support this viewpoint, fatty acids, alkanols, and alkanediols were chosen as typical HOCs, and their chemical stability was determined by the $K_2Cr_2O_7$ oxidation method. The carbon loss rate of HOCs was significantly negatively correlated with the Log*P* value ($n = 11$, $r = -0.867$, $p = 0.001$) (Fig. 3d), indicating that the greater the Log*P* value of HOCs, the stronger their chemical stability. Because the *I* value of the hydrophobic coating was calculated based on the Log*P* value, a higher hydrophobic intensity implies that the coating had greater stability and provided greater protection. Among the four kinds of leaf-derived hydrochars, the carbon loss rate differed significantly between CL-H and PN-H. The carbon loss rate of PN-H was 15.50% lower than that of CL-H, indicating that the chemical stability of PN-H was higher than that of CL-H. Because the difference in SSA between CL-H and PN-H was not obvious, and their aromaticity was similar, the difference in chemical stability between these two hydrochars was attributed mainly to the hydrophobic coating of PN-H exhibiting a 36.35% higher hydrophobic intensity than that of CL-H.

After acetone extraction, the carbon loss rate of CL-H did not significantly change, whereas those of LL-H, PL-H, and PN-H increased significantly, ranging from 10.13% to 16.01%, indicating a significant decrease in chemical stability. LL-H exhibited the greatest increase in carbon loss rate, as its hydrophobic coating had

https://doi.org/10.48130/ebp-0026-0012

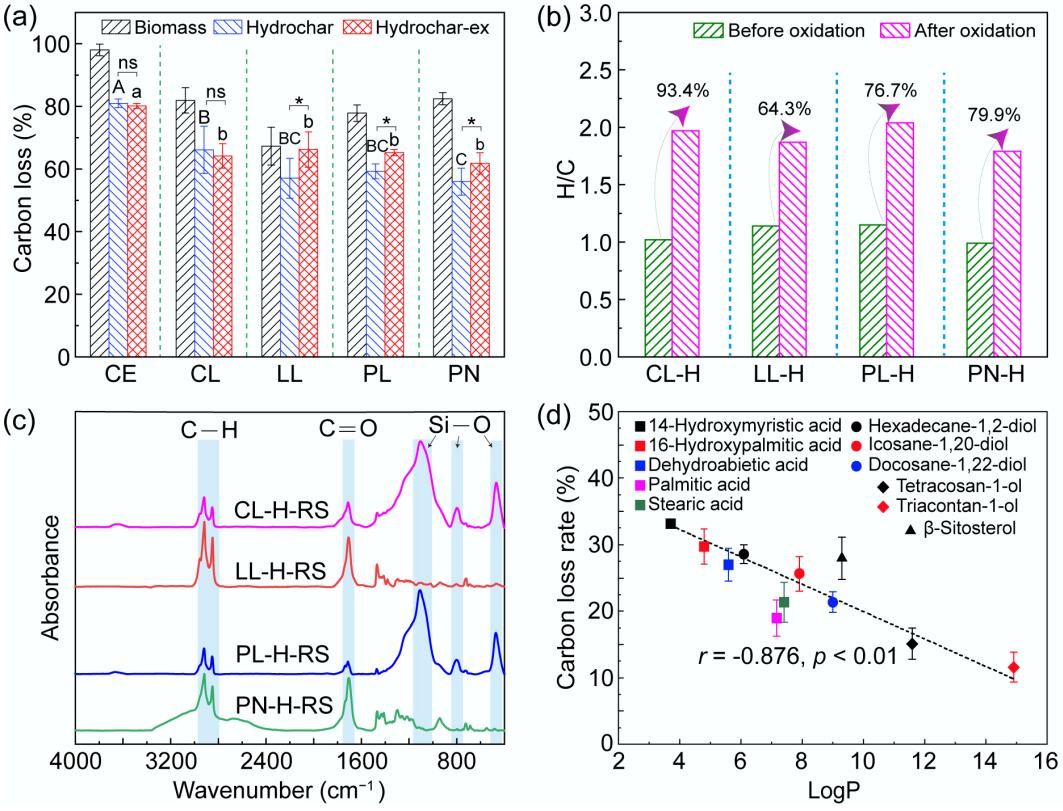

Fig. 3 (**a**) Carbon loss rate of hydrochar oxidized by $K_2Cr_2O_7$ before and after acetone extraction. (**b**) H/C atomic ratio of leaf-derived hydrochar before and after oxidation by $K_2Cr_2O_7$. (**c**) FTIR spectra of solid residues obtained from the chemical oxidation of leaf-derived hydrochar. (**d**) Correlation between Log*P* values of hydrophobic organics and their carbon loss rate after oxidation by $K_2Cr_2O_7$. Sample abbreviations CE, CL, LL, PL, and PN are consistent with Fig. 2; hydrochar-related labels CE-H, CL-H, LL-H, PL-H, and PN-H follow the definitions provided in Fig. 1, and the labels Hydrochar and Hydrochar-ex are defined in Fig. 2. CL-H-RS, LL-H-RS, PL-H-RS, and PN-H-RS denote solid residues obtained from chemical oxidation of CL-H, LL-H, PL-H, and PN-H hydrochar, respectively. Log*P* is the logarithmic value of the octanol-water partition coefficient *P*. (**A**)–(**C**) present a comparison of the carbon loss rates of different hydrochars before extraction, and (**a**)–(**c**) present a comparison of carbon loss rates of different hydrochars after extraction. ns indicates no significant difference in the carbon loss rate of hydrochar before and after extraction, and * indicates a significant difference in the carbon loss rate of hydrochar before and after extraction ($p < 0.05$).

the highest hydrophobic intensity and provided the greatest protection. Consequently, when the hydrophobic coating was removed, the reduction in chemical stability of LL-H was the most pronounced. It is important to note that while the difference in hydrophobic intensity between the hydrophobic coatings of CL-H and PL-H was minor, the chemical stability of CL-H remained unchanged after acetone extraction, whereas that of PL-H decreased significantly. This discrepancy may be attributed to the greater increase in SSA of PL-H (323.8%) compared with CL-H (70.78%) after the removal of the hydrophobic coating, both relative to their respective pre-extraction values. An increase in SSA made more reactive sites accessible to oxidizing agents, thereby reducing the chemical stability of hydrochar. In comparison, the coating constructed a continuous protective film over hydrochar particles. It blocked surface pores and covered exposed reactive sites, restricting the diffusion of oxidizing agents[9,31]. This effect reduced reactant collision frequency and weakened chemical reactivity, thus enhancing hydrochar stability. Notably, when the four kinds of leaf-derived hydrochars were compared after acetone extraction, no significant difference was found in their carbon loss rates. This suggests that, after the removal of the hydrophobic coating, the chemical stability of hydrochars tended to converge. Therefore, the variations in the chemical stability of hydrochars derived from different biomasses were primarily attributed to the protective effect of the hydrophobic coating.

Conclusions

The hydrophobic coating of LL-H exhibited the highest hydrophobic intensity, with its main component being nonacosane-4,10-diol derived from the wax. The main components of the hydrophobic coatings in CL-H, PL-H, and PN-H were palmitic acid or 16-hydroxypalmitic acid, which were degradation products of cutin. A significant positive correlation was observed between the hydrophobic intensity of the hydrophobic coating and the alkyl carbon content in the bulk hydrochar. The hydrophobic alkyl carbon coating reduced the activation energy and pre-exponential factor of thermal decomposition without changing the hydrochar's thermal stability. The protective effect on the hydrochar's chemical stability increased with the hydrophobic intensity of the coating. After losing the barrier effect of the hydrophobic coatings, the carbon loss rate of hydrochar oxidized by $K_2Cr_2O_7$ increased by 10.13%–16.01%. Therefore, the hydrophobic alkyl carbon coating may strengthen hydrochar stability in soil, which is expected to promote its capacity for soil carbon sequestration.

Supplementary information

It accompanies this paper at: https://doi.org/10.48130/ebp-0026-0012.

Ethical statements

Not applicable.

Author contributions

The authors confirm their contributions to the paper as follows: Jianping Fan: conceptualization, methodology, investigation, data curation, writing – original draft, funding acquisition; Fangfang Li: conceptualization, methodology, writing – review & editing, funding acquisition; Qingkong Chen: validation, formal analysis, writing – original draft; Peiwen Zeng: investigation, writing – original draft; Yanlin Li: data curation, visualization, funding acquisition; Wei Chen: resources, funding acquisition; Qiangbin Yang: resources, funding acquisition; Hong Yang: conceptualization, supervision, writing – review & editing. All authors reviewed the results and approved the final version of the manuscript.

Data availability

The datasets generated during and/or analyzed in the current study are available from the corresponding author on reasonable request.

Acknowledgments

Not applicable.

Funding

This work was supported by the National Natural Science Foundation of China (42267028, 42130711, 42007352, and 32101394), the Chongqing Natural Science Foundation (CSTB2022NSCQ-MSX1107), and the Project of Chongqing University of Arts and Sciences (P2021HH04).

Declarations

Competing interests

The authors declare that they have no conflict of interest.

Author details

[1]Chongqing Key Laboratory for Resource Utilization of Heavy Metal Wastewater, Chongqing University of Arts and Sciences, Chongqing 402160, China; [2]Yunnan Provincial Key Laboratory of Soil Carbon Sequestration and Pollution Control, Faculty of Environmental Science & Engineering, Kunming University of Science & Technology, Kunming 650500, China; [3]School of River and Engineering, Chongqing Jiaotong University, Chongqing 400074, China; [4]Department of Geography and Environmental Science, University of Reading, Reading, RG6 6AB, UK

References

[1] Deng X, Teng F, Chen M, Du Z, Wang B, et al. 2024. Exploring negative emission potential of biochar to achieve carbon neutrality goal in China. *Nature Communications* 15:1085

[2] Malghani S, Gleixner G, Trumbore SE. 2013. Chars produced by slow pyrolysis and hydrothermal carbonization vary in carbon sequestration potential and greenhouse gases emissions. *Soil Biology and Biochemistry* 62:137–146

[3] Harvey OR, Kuo LJ, Zimmerman AR, Louchouarn P, Amonette JE, et al. 2012. An index-based approach to assessing recalcitrance and soil carbon sequestration potential of engineered black carbons (biochars). *Environmental Science & Technology* 46:1415–1421

[4] Gómez N, Rosas JG, Singh S, Ross AB, Sánchez ME, et al. 2016. Development of a gained stability index for describing biochar stability: relation of high recalcitrance index (R50) with accelerated ageing tests. *Journal of Analytical and Applied Pyrolysis* 120:37–44

[5] Zhang X, Yang X, Yuan X, Tian S, Wang X, et al. 2022. Effect of pyrolysis temperature on composition, carbon fraction and abiotic stability of straw biochars: correlation and quantitative analysis. *Carbon Research* 1:17

[6] Yang F, Xu Z, Yu L, Gao B, Xu X, et al. 2018. Kaolinite enhances the stability of the dissolvable and undissolvable fractions of biochar via different mechanisms. *Environmental Science & Technology* 52:8321–8329

[7] Cross A, Sohi SP. 2013. A method for screening the relative long-term stability of biochar. *GCB Bioenergy* 5:215–220

[8] Chen D, Yu X, Song C, Pang X, Huang J, et al. 2016. Effect of pyrolysis temperature on the chemical oxidation stability of bamboo biochar. *Bioresource Technology* 218:1303–1306

[9] Leng L, Huang H. 2018. An overview of the effect of pyrolysis process parameters on biochar stability. *Bioresource Technology* 270:627–642

[10] Pan T, Guo Z, Zhang X, Feng L. 2024. Hydrothermal carbonization of biomass waste and application of produced hydrochar in organic pollutants removal. *Journal of Cleaner Production* 457:142386

[11] Lozano EJ, Martín-Lara MÁ, Blázquez G, Muñoz-Batista MJ, Calero M. 2026. Enhancing biomass properties for biofuels: a comparative analysis of pyrolysis and hydrothermal carbonization technologies. *Journal of Analytical and Applied Pyrolysis* 193:107435

[12] Cognigni P, Leonelli C, Berrettoni M. 2025. A bibliographic study of biochar and hydrochar: differences and similarities. *Journal of Analytical and Applied Pyrolysis* 187:106985

[13] Fan J, Li F, Fang D, Chen Q, Chen Q, et al. 2022. Effects of hydrophobic coating on properties of hydrochar produced at different temperatures: specific surface area and oxygen-containing functional groups. *Bioresource Technology* 363:127971

[14] Luo X, Du H, Du J, Zhang X, Xiao W, et al. 2024. The influence of biomass type on hydrothermal carbonization: role of calcium oxalate in enhancing carbon sequestration of hydrochar. *Journal of Environmental Management* 349:119586

[15] Yeats TH, Rose JKC. 2013. The formation and function of plant cuticles. *Plant Physiology* 163:5–20

[16] Sriram A, Swaminathan G. 2018. Pyrolysis of *Musa balbisiana* flower petal using thermogravimetric studies. *Bioresource Technology* 265:236–246

[17] Oyeleke OR, Hu Y, Naterer GF. 2025. Effects of potassium salt on cellulose pyrolysis: biochar production, kinetic triplet, and thermodynamic properties. *Chemical Engineering Science* 313:121787

[18] Choi W, Tuteja A, Mabry JM, Cohen RE, McKinley GH. 2009. A modified Cassie–Baxter relationship to explain contact angle hysteresis and anisotropy on non-wetting textured surfaces. *Journal of Colloid and Interface Science* 339:208–216

[19] Jing W, Su M, Yang K, Kang Q, Li Y, et al. 2026. Dynamic contact angle as a new metric for the water repellency evaluation of biochar-amended soil. *Biochar* 8:38

[20] Ensikat HJ, Ditsche-Kuru P, Neinhuis C, Barthlott W. 2011. Superhydrophobicity in perfection: the outstanding properties of the lotus leaf. *Beilstein Journal of Nanotechnology* 2:152–161

[21] González-Valenzuela L, Renard J, Depège-Fargeix N, Ingram G. 2023. The plant cuticle. *Current Biology* 33:R210–R214

[22] Fernández V, Guzmán-Delgado P, Graça J, Santos S, Gil L. 2016. Cuticle structure in relation to chemical composition: re-assessing the prevailing model. *Frontiers in Plant Science* 7:427

https://doi.org/10.48130/ebp-0026-0012

[23] Yabalak E, Akay S, Kayan B, Gizir AM, Yang Y. 2023. Solubility and decomposition of organic compounds in subcritical water. *Molecules* 28:1000
[24] Madeira PP, Todorov G, Uversky VN, Zaslavsky BY. 2024. Solvent polarity and hydrophobicity of solutes are two sides of the same coin. *Biochemical and Biophysical Research Communications* 701:149600
[25] de Sousa FF, Nogueira CES, Freire PTC, Moreira SGC, Teixeira AMR, et al. 2016. Conformational change in the C form of palmitic acid investigated by Raman spectroscopy and X-ray diffraction. *Spectrochimica Acta Part A: Molecular and Biomolecular Spectroscopy* 161:162–169
[26] Ivanova EP, Nguyen SH, Guo Y, Baulin VA, Webb HK, et al. 2017. Bactericidal activity of self-assembled palmitic and stearic fatty acid crystals on highly ordered pyrolytic graphite. *Acta Biomaterialia* 59:148–157
[27] Esperança ES, Bonatto MS, Costa MC, Meirelles AJA, Maximo GJ. 2022. Cholesterol thermodynamic behaviour in mixtures with medium chain fatty acids and vegetable oils composed of them. *Fluid Phase Equilibria* 557:113432
[28] Bayard M, Kauffmann B, Leal-Calderon F, Cansell M. 2024. Palmitic acid at high concentration modifies the nanoscale structure of anhydrous milk fat. *Food Chemistry* 443:138522
[29] Bayard M, Leal-Calderon F, Cansell M. 2017. Free fatty acids and their esters modulate isothermal crystallization of anhydrous milk fat. *Food Chemistry* 218:22–29
[30] de Jager M, Schröter F, Wark M, Giani L. 2022. The stability of carbon from a maize-derived hydrochar as a function of fractionation and hydrothermal carbonization temperature in a Podzol. *Biochar* 4:52
[31] Yang H, Yu Y, Zhang H, Wang W, Zhu J, et al. 2024. Effect mechanism of phosphorous-containing additives on carbon structure evolution and biochar stability enhancement. *Biochar* 6:39
[32] Sawisai R, Wanchanthuek R, Radchatawedchakoon W, Sakee U. 2019. Simple continuous flow synthesis of linoleic and palmitic acid-coated magnetite nanoparticles. *Surfaces and Interfaces* 17:100344
[33] Prudnikov E, Polishchuk I, Sand A, Abu Hamad H, Massad-Ivanir N, et al. 2023. Self-assembled fatty acid crystalline coatings display superhydrophobic antimicrobial properties. *Materials Today Bio* 18:100516
[34] Zhuang X, Zhan H, Song Y, He C, Huang Y, et al. 2019. Insights into the evolution of chemical structures in lignocellulose and non-lignocellulose biowastes during hydrothermal carbonization (HTC). *Fuel* 236:960–974
[35] Yu F, Zhu X, Jin W, Fan J, Clark JH, et al. 2020. Optimized synthesis of granular fuel and granular activated carbon from sawdust hydrochar without binder. *Journal of Cleaner Production* 276:122711
[36] Singh BP, Cowie AL, Smernik RJ. 2012. Biochar carbon stability in a clayey soil as a function of feedstock and pyrolysis temperature. *Environmental Science & Technology* 46:11770–11778
[37] Yu L, Shi X, Zhang S, Zhang Q, Chen W. 2025. A comprehensive investigation of kinetic and thermodynamic analysis to catalytic pyrolysis bamboo with N-doped biochar. *Fuel* 396:135312
[38] Lin H, Li Q, Zhang S, Zhang L, Hu G, et al. 2022. Involvement of the organics in aqueous phase of bio-oil in hydrothermal carbonization of lignin. *Bioresource Technology* 351:127055
[39] Cimò G, Kucerik J, Berns AE, Schaumann GE, Alonzo G, et al. 2014. Effect of heating time and temperature on the chemical characteristics of biochar from poultry manure. *Journal of Agricultural and Food Chemistry* 62:1912–1918
[40] Kaur R, Gera P, Jha MK, Bhaskar T. 2018. Pyrolysis kinetics and thermodynamic parameters of castor (*Ricinus communis*) residue using thermogravimetric analysis. *Bioresource Technology* 250:422–428
[41] Yuan X, He T, Cao H, Yuan Q. 2017. Cattle manure pyrolysis process: kinetic and thermodynamic analysis with isoconversional methods. *Renewable Energy* 107:489–496
[42] Han L, Ro KS, Wang Y, Sun K, Sun H, et al. 2018. Oxidation resistance of biochars as a function of feedstock and pyrolysis condition. *Science of the Total Environment* 616–617:335–344